

Chapter 5

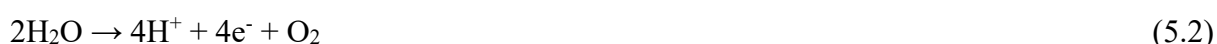
*In Situ Defect Engineering of HfS₂, HfSe₂
and Janus HfSSe for Highly Efficient
Hydrogen Evolution Reaction: An Ab Initio
Study*

5.1 Introduction

Human survival and advancement are entirely dependent on energy in the current era [1-4]. However, the rising need for energy and the increasing depletion of non-renewable fossil fuels, as well as the harmful consequences of these fossil fuels on the environment, prompted a search for alternative sources of energy such as biomass, geothermal, solar, hydro, and tidal energy [5-8]. Because of its high gravimetric specific energy density and environmentally favorable properties, H energy is being seen as one of the most appealing alternatives to fossil fuels among all clean energy sources available [9,10]. H is not only regarded as a clean energy source, but it is also used in the chemical industry for the production of ammonia and methanol, and it has multiple potential uses such as fuelling automobiles, fuel cells, heating, aircraft, and sulfur elimination from petroleum [11-13]. Owing to the high energy sustainability norms, conventional hydrogen production is not as appealing. As a result, the development of environmentally friendly technologies to improve the hydrogen economy is critical [14]. Among the several ways of generating hydrogen, the electrochemical splitting of water (using a photocatalyst/electrocatalyst/photoelectron catalyst) has drawn a lot of attention because of its carbon-free hydrogen creation [15-20]. H₂ is a product of water electrolysis, and catalysts play an important part in this process [21]. In this method, the water splitting procedure can be subdivided into two half-reactions: the evolution of H₂ that is represented by [22],



and evolution of oxygen gas O₂ that is,



HER is typically a two-electron transfer mechanism involving a catalytic intermediate. This reaction is known as Volmer reaction. Noble metals like Pt, Pd, Au, and Ag, for example,

exhibit a remarkable ability to catalyze the electrochemical production of hydrogen with low overpotential values. [22,23], however, their steep costs and unavailability are significant limitations. As a result, finding earth-rich HER catalysts with minimal overpotentials is highly sought after [24-27]. TMDs have gained acknowledgement for being cost-effective and depicting impressive HER performance. [28-38]. At high current densities, the HER performance of 2D TMD electrocatalysts has been found to be superior to that of commercial benchmark Pt/C catalysts, which is a favourable factor in commercial hydrogen production [39,40]. 2D TMDs have an MX₂ molecular structure, where M is a transition metal atom (e.g., Mo, W, Zr, Sn, etc.) and X is a chalcogen atom (e.g., S, Se, and Te). TMDs exist in a wide range of structural phases, the most frequent of which are 2H and 1T [22]. It exhibits a wide range of electrical, magnetic, and optical properties due to the diversity of its structural phases [22]. Many 2D TMDs, such as MoS₂, WS₂, and SnSe₂, have sparked intense interest due to their inexpensive cost of production and superior electrocatalytic performance [41]. However, it has been discovered that the basal plane of TMDs is not as reactive as the edge sites, limiting its maximal utilization. There are numerous techniques to improve this disadvantage, including doping, defect, and strain application.

Defects in two-dimensional (2D) materials includes edge defects, topological defects, vacancies, and dopant-derived defects. They are important in electrocatalysis since they frequently function as active sites that actively participate in chemical processes. Defects can also affect the electrical structure of active sites, allowing more catalytic sites to be exposed to the electrolyte [42-45]. As a result, defect engineering has emerged as a viable method for fine-tuning electrocatalytic performance [46,42-43]. Among the extensively used materials, HfX₂ (where X = S, Se, Te) combinations have received a lot of attention [47-55]. The study's findings show that the HfX₂ structure has a low bandgap and movement, making it a good option for electrical and optoelectronic uses [56-64]. Toh et al. [47-49] described the

electrochemical activation of ZrSe₂ and HfSe₂ towards HER by both oxidation and reduction. Also investigated is the increase of structural, electrical, and optical characteristics of HfS₂ monolayers via lathanide atom doping [50-52]. There have been numerous investigations on the janus structure of S and Se in HfSe₂ for use in electronic devices [53-55]. This demonstrates the materials' wide range of uses, which prompted us to study the characteristics of all three structures, HfSe₂, HfS₂, and HfSSe, using defect engineering. Several studies have shown promise in enhancing the catalytic efficiency of janus materials using defect engineering techniques. Dequan et al., [65] for example, evaluated the impact of intrinsic strain caused by the janus structure as well as the significance of voids in triggering the inert basal plane. In the WSSe system, they discovered an ideal hydrogen adsorption-free energy (ΔG^H) close to thermoneutrality, yielding high HER catalytic efficiency under strain-free circumstances with S/Se vacancies at their inherent concentrations. Furthermore, Yadong et al. [66] used first-principles computations to investigate the structural, electrical, optical, and photocatalytic capabilities of developing elements like MoSi₂N₄, in addition to proposed janus structures like MoSiGeN₄ and WSiGeN₄. Their findings supported the janus structure's stability.

In the present work, multiple characteristics including structural and electronic have been studied in addition to the catalytic performance of each of the structures, namely HfS₂, HfSe₂ and Janus HfSSe, in pristine form, and changes in their characteristics after the development of various defects. All computations are carried out using the dispersion-corrected density functional theory (DFT) method.

5.2 Computational Methods

5.2.1 Computational Details

The structural, electronic and catalytic properties for pristine and defected HfS₂, HfSe₂ and Janus HfSSe were analyzed using the state-of-art first-principles based DFT. The Quantum Espresso software was implemented for the study [67]. The generalized gradient approximation (GGA) proposed by Perdew-Burke-Ernzerhof (PBE) was used for the exchange correlation interaction [68]. To obtain the accurate value of adsorption energy for H adsorption, the dispersion correction (D2) of Grimme was employed [69]. Here, we have created a 3x3x1 supercell of the monolayers so that we have sufficient area to obtain acceptable results. The kinetic energy and charge density cut-offs are 80 and 800 Ry respectively which are sufficient to fully converge lattice parameters and total energy. To avoid interaction between two successive layers, a 15 Å distance is inserted perpendicular to monolayers. The dense grid of 7x7x1 was employed for the reciprocal space which is constructed under Monkhorst-Pack scheme [70]. The smearing of Marzari-Vanderbilt is employed for required calculations. The energy convergence value of 10⁻⁴ eV was set and the convergence was carried out self consistently until the maximum Hellmann-Feynman force acting on each atom is lower than 0.001 eV/ Å. The Kohn-Sham equation was used to obtain the convergence threshold of 1x10⁻⁸ Ry that used iterative Davidson type diagonalization approach.

5.2.2 Theoretical Formulations

The Sabatier principle is used to investigate the HER activity of pristine and defected HfS₂, HfSe₂ and Janus HfSSe monolayers [5-8]. The Sabatier principle states that the interaction between the catalyst and intermediate should neither be strong nor weak. At equilibrium condition, efficiency of HER activity is determined using exchange current density that is related to the Gibbs free energy (ΔG^H) [71-73] at (pH=0) that is defined as,

$$\Delta G^H = \Delta E_{\text{ads}}^H + E^{\text{ZPE}} - T\Delta S \quad (5.3)$$

Here, $\Delta E_{\text{ads}}^{\text{H}}$ is the adsorption energy of H atom and E^{ZPE} represents the zero-point energy difference of atom in the adsorbed and gas phase. The entropy correction is ΔS . For HER, the value of $E^{\text{ZPE}} - T\Delta S$ is 0.24 eV as it is evident from the literatures [71-73]. For H adsorption, equation (5.3) takes the form of $\Delta G^{\text{H}} = \Delta E_{\text{ads}}^{\text{H}} + 0.24$ [71-73]. The H adsorption energy is denoted as,

$$\Delta E_{\text{ads}}^{\text{H}} = E(\text{system} + \text{H}) - E(\text{system}) - \frac{1}{2} E(\text{H}_2) \quad (5.4)$$

Where, $E(\text{system} + \text{H})$ is the total energy of H adsorbed pristine and defected monolayers, $E(\text{system})$ is the energy of pristine and defected monolayers before adsorption, $E(\text{H}_2)$ is the energy of isolated H molecule. Pt as considered the best catalyst has ΔG^{H} close to zero. Thus, for a catalyst to provide satisfactory results, the ΔG^{H} should be close to that of Pt. If the value of ΔG^{H} is positive, it implies that the binding is weak making the adsorption difficult and on the other side if ΔG^{H} is negative, it implicates that the binding is strong that hurdles the desorption process. Thus, we require an optimal value of ΔG^{H} for excellent catalytic activity of HER. There are two other descriptors for HER activity, the overpotential and exchange current density that is defined as,

$$\eta = \Delta G^{\text{H}} / e \quad (5.5)$$

$$i_0 = -eK_0 \frac{1}{1 + e^{\frac{|\Delta G^{\text{H}}|}{K_B T}}} \quad (5.6)$$

Here, e is electron charge, K_B is Boltzmann constant (eV/K), $T=298$ K and rate constant $K_0 = 1 \text{ (s}^{-1}\text{) (site}^{-1}\text{)}$.

5.3 Results and Discussion

The ground state properties of 3x3x1 HfS₂, HfSe₂ and HfSSe under pristine and modified conditions was investigated to get insight to the effect of chemically and structurally

modified system on their catalytic properties. When considering Janus HfSSe, a unique scenario arises where one of the chalcogen layers within the original HfX₂ TMD monolayer is substituted with a layer containing atoms of a different type. One can replace any of the chalcogen atom with the other one and vice-versa. The substitution or change made to the structural geometry has a noticeable impact on the behaviour of the system of interest; since any of the aforementioned modification ultimately modifies the chemical environment of the system that in turn causes noticeable alterations in its properties. Specifically, the change disrupts the symmetry of the structure, making it less balanced or isotropic. This loss of balance affects the overall symmetry of the system, meaning that the structure as a whole is no longer as symmetrical having P-3m1 space group as prior to the substitution. The top and side views of the HfS₂, HfSe₂ and Janus HfSSe are pictorially represented in **Figure 5.1**. The optimized lattice constants for the monolayers HfS₂, HfSe₂ and HfSSe are 10.99 Å, 11.22 Å and 11.11 Å, respectively, that are in agreement with the previously reported studies [75-76]. The interatomic bond-lengths are found to be 2.56 Å and 2.68 Å, respectively for Hf-S and Hf-Se pairs, and for Janus HfSSe system, the bond-lengths of the said pairs are 2.56 Å and 5.69 Å, respectively (See **Table 5.1**) [76]. The DFT calculated electronic band structure of pristine HfS₂, HfSe₂ and Janus HfSSe are represented in **Figure 5.2**. The highest occupied energy level, known as the valence band maxima (VBM), is situated at the high symmetry point Γ of the Brillouin zone for all three cases. Conversely, the lowest energy level in the conduction band, referred to as the conduction band minima (CBM), is located at the high symmetry point M of the Brillouin zone indicating indirect nature of the bandgap. The magnitude of the band gap of HfS₂, HfSe₂ and Janus HfSSe is found to be 1.56 eV, 0.68 eV and 1.04 eV, respectively. These values are in accordance with the reported data [76]. As expected, the Janus HfSSe exhibits band gap lying between the magnitudes of HfS₂ and HfSe₂. The reduction in the band gap can be foreseen due to the incorporation of Se atoms in place of S atom. Since the band gap of both HfS₂ and HfSSe

lies in the range of 1-2 eV suggesting their, probable utility as a photo-catalyst; whereas, HfSe₂ can be beneficial to be tested for electro-catalytic application. As discussed earlier, Pt has been reported to be an excellent candidate for an HER catalyst, but its scarce availability limits its largescale application. However, the search for cost-effective and feasibly available catalysts is a high priority demand.

It has been observed that the edge sites of the TMDs is gives pronounced catalytic activity as compared to the basal plane [81]. Therefore, we have studied H adsorption on various sites of these pristine structures. **Figure 5.3** depicts the optimized structures after H-adsorption over HfS₂, HfSe₂ and HfSSe. We have calculated $\Delta E_{\text{ads}}^{\text{H}}$ and ΔG^{H} (See **Table 5.2**) at various sites of these monolayers using equation (5.3) and (5.4). Here, it can be validated that the, in case of HfS₂ the S edge adsorption shows better catalytic activity as compared to basal plane. Similarly, in case of HfSe₂ we observe the same trend of active edge site as compared to its basal plane. Also, it is evident that HfS₂ has better catalytic efficiency than HfSe₂. Similar trend has been observed in case of ZrS₂ and ZrSe₂ as well [82]. Additionally, when we contrast HfS₂ with HfSe₂, we observe that the S edge exhibits higher reactivity in comparison to the Se edge. Interestingly, this differs from the general trend seen in TMDs, where Se-based catalysts tend to be more active than their S counterparts [81]. In the context of Janus structures, there exist two distinct edge sites: one constituting the sulfur atoms, which is referred as the S-edge, and the other consisting selenide atoms, known as the Se-edge. It is evident that because of the asymmetric arrangement of the host atoms under Janus configurations, there is an augmentation in catalytic activity specifically at the edges. Additionally, it's worth noting that Janus structures exhibit a rather unconventional trend, where the S edge site displays higher reactivity compared to the Se edge. Finally, we can evaluate from comparison of ΔG^{H} of all three systems at basal plane and edge site, which yields us the following sequence SHfSe > HfS₂ > HfSe₂ where SHfSe refers to the hydrogen adsorption at S-edge site of Janus HfSSe. The Janus structure

yields good catalytic activity for HER, as observed in Janus SeMoS [83]. The H adsorption is in following sequence $\text{HfSSe} > \text{HfS}_2 > \text{HfSe}_2$. To get atomic level insights to the dynamics, we analyzed the computed Löwdin charges that explains the observed trend. From **Table 5.2**, we can clearly observe the enhancement in the charge of H atom that can be attributed charge transfer from the host material. If ΔQ_{H} (e) (difference in charge hydrogen before and after adsorption) is found to be positive, then the charge transfer has occurred from the system to hydrogen and vice-versa. Comparing the ΔQ_{H} of HfS_2 and HfSe_2 , ΔQ_{H} is higher for HfS_2 which is the reason that HfS_2 can be suggested as a better HER catalyst. However, in the case of the Janus configuration, due to charge redistribution of S and Se atoms that occurs due to asymmetric arrangement, the ΔQ_{H} value for Se site is found to be higher than S site, which is the root cause for the enhancement in the Se site activity. The Löwdin charge analysis validates the results obtained from the ΔG^{H} and $\Delta E_{\text{ads}}^{\text{H}}$. We observed, there is higher transfer at basal plane compared to edge sites which leads to strong interaction with hydrogen ion, this may cause hindrance for the evolution of the hydrogen gas. Further, we conducted an analysis of the total and PDOS for H adsorption on various configurations for all three systems. Following the adsorption of H onto these pristine systems, they exhibited metallic properties, confirming a notable interaction between H and the catalyst materials. The PDOS analysis revealed that the hydrogen atoms contribution, particularly in the vicinity of the Fermi level, can be attributed to weak interaction towards H. **Figure 5.4** shows the PDOS of the three systems providing good catalytic efficiency as S-site HfS_2 , Se-site HfSe_2 and S-edge site HfSSe . In case of pristine HfS_2 , the contribution of H atom is more towards the CBM indicating physisorption; whereas, in case of pristine HfSe_2 , the contribution of H atom is also more towards the CBM providing same analysis of physisorption as HfS_2 . In case of Janus HfSSe , the contribution of H atom has a small peak near conduction band indicating physisorption. On the other hand, the interaction of hydrogen state with adsorbate states gives rise to bonding and anti-bonding states

which can be attributed to feeble interaction with hydrogen atoms that can be beneficial for desorption of hydrogen. It can be concluded from the previous discussion that the edge sites of HfS₂ and HfSe₂ are more active as compared to basal plane but among the three pristine systems S-edge site of HfSSe shows better HER catalytic activity. In the past, there was a prevailing notion that the active edge sites of TMD catalysts posed a significant obstacle to efficient H₂ production [14,84,27]. As a result, a potential solution to this challenge has been suggested: by enhancing the reactivity of the basal plane, it could help overcome this issue. One of the most common known method to improve the activity of basal plane is by introducing various defects that have previously shown increment in catalytic efficiency [42-45]. Thus, we can consider the possibility of enhancement of catalytic efficiency of HfS₂, HfSe₂ and Janus HfSSe by defect creation. We have investigated the effect of defected monolayers towards the HER performance. In case of HfS₂, we have created two vacancies, monohafnium vacancy (V_{Hf}) and monosulphur vacancy (V_S). For HfSe₂, we have created monohafnium vacancy (V_{Hf}) and monoselenium vacancy (V_{Se}). For Janus HfSSe, we have created three vacancies, monohafnium vacancy (V_{Hf}), monosulphur vacancy (V_S) and monoselenium vacancy (V_{Se}) respectively. All the different vacancies are denoted in **Figure 5.5**. Since in practice, it is impossible to get 100% pure and defect free system; therefore, the defect creation can be an efficient method to finely adjust the essential electronic characteristics of the material. This serves as a fundamental strategy to elevate the catalytic performance of a catalyst. After thorough optimization of various functionalized systems, we observed that there were minimal alterations in the overall structure. After the creation of defects in HfS₂, HfSe₂ and HfSSe structures, it is observed that the lattice constants of the systems decrease (See in **Table 5.3**), which is attributed to the fact the ions around these vacancies relax inwardly as observed in various previous studies [85]. To assess the improvement in the HER activity of defected systems, we introduced H onto the defect sites shown in **Figure 5.6**. Subsequently, we

calculated the $\Delta E_{\text{ads}}^{\text{H}}$ and determined the ΔG^{H} for defected monolayers, utilizing equation (5.3) and (5.4). We have observed that defect engineering has indeed enhanced the catalytic efficiency as seen from the obtained $\Delta E_{\text{ads}}^{\text{H}}$ and ΔG^{H} values denoted in **Table 5.3**. Here, we can analyze that in case of HfS₂, V_{Hf} gives us lower ΔG^{H} as compared to V_S and its parent structure. Further, in case of HfSe₂, it is observed that, V_{Hf} gives lower ΔG^{H} as compared to V_{Se} and its parent structure. Whereas, in case of Janus HfSSe, the order of lowest ΔG^{H} is for V_{Hf}, followed by V_{Se} and V_S. Also, we can conclude that defected HfS₂ gives us the lowest ΔG^{H} followed by defected HfSe₂ and defected Janus HfSSe with values 0.03 eV, 0.21 eV and 0.25 eV, respectively. From the above discussion we can conclude that V_{Hf} in case of HfS₂ is best-suited for HER as its value is closer to zero which is the ideal value. Finally, it can be concluded that the defected systems help to increase basal plane activity of TMDs. The electronic properties of defected HfS₂, HfSe₂ and Janus HfSSe systems is calculated for mapping the difference in the properties of interest. The **Figure 5.7** represents the PDOS plot for the system possessing lowest ΔG^{H} . It is observed that all the systems after H-adsorption become metallic in nature. The presence of H atom near the Fermi level in the PDOS suggests their involvement in bond formation with the adsorbate. Additionally, it can be observed that in case of HfS₂, the PDOS of H exhibits higher density in the conduction band. A similar pattern is observed in the PDOS of HfSe₂ in case of V_{Hf} at hollow site and HfSSe as shown in **Figure 5.7**. This phenomenon aligns with the nature of optimal interaction, which is consistent with our findings from ΔG^{H} calculations. However, when H states interact with adsorbate states, it contributes in both bonding and anti-bonding states. These states indicate a weaker interaction with H atom, making it easier for them to desorb from the system. Furthermore, the Löwdin charge analysis, we observed the chalcogenide (S or Se) defect leads to higher charge transfer as compared to the hafnium defect as seen from **Table 5.3**. Thereafter, we have compared the ΔG^{H} of our work with the previously reported TMDS, in the volcano plot (**Figure 5.8**). We found that not only

basal activity of Hf-defected HfS₂ increases but falls in the best catalyst shaded region followed by other two defected system HfSe₂-V_{Hf}-Hollow site and HfSSe-V_{Hf}-S site. There ΔG^H comparable to CoS₂, CrS₂, FeS₂, Co-doped HfS₂, P-doped HfS₂ TMDs [86]. **Table 5.4** shows the comparison of ΔG^H of all stable 2D-TMDs with HfS₂ and HfSe₂ monolayers.

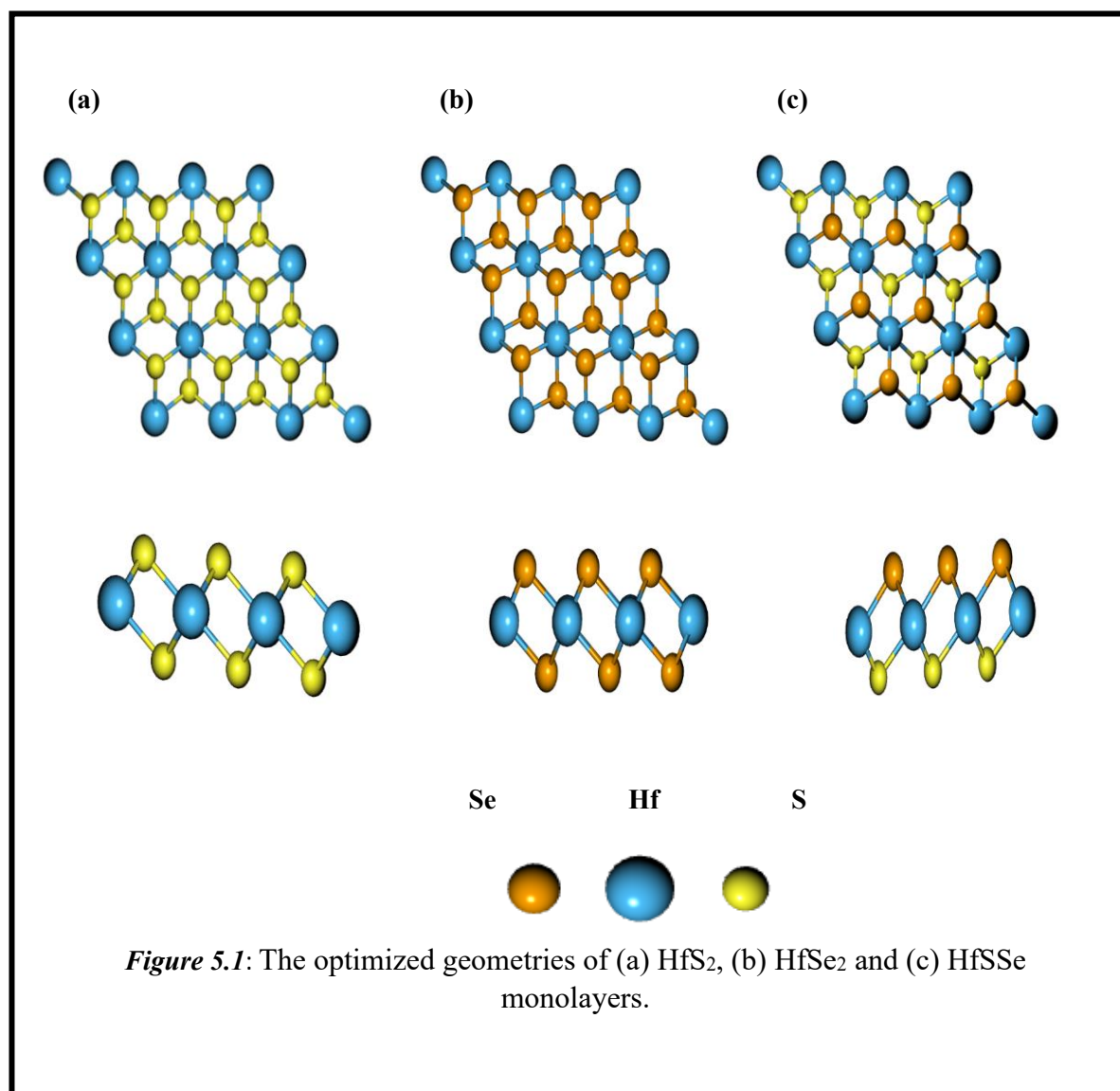


Table 5.1: Calculated lattice and bond lengths of HfS₂, HfSe₂ and HfSSe monolayers.

Systems	Lattice (Å)	Bond length (Å)
HfS ₂	10.99	2.56
HfSe ₂	11.22	2.68
HfSSe	11.11	2.56 (Hf-S) 5.69 (Hf-Se)

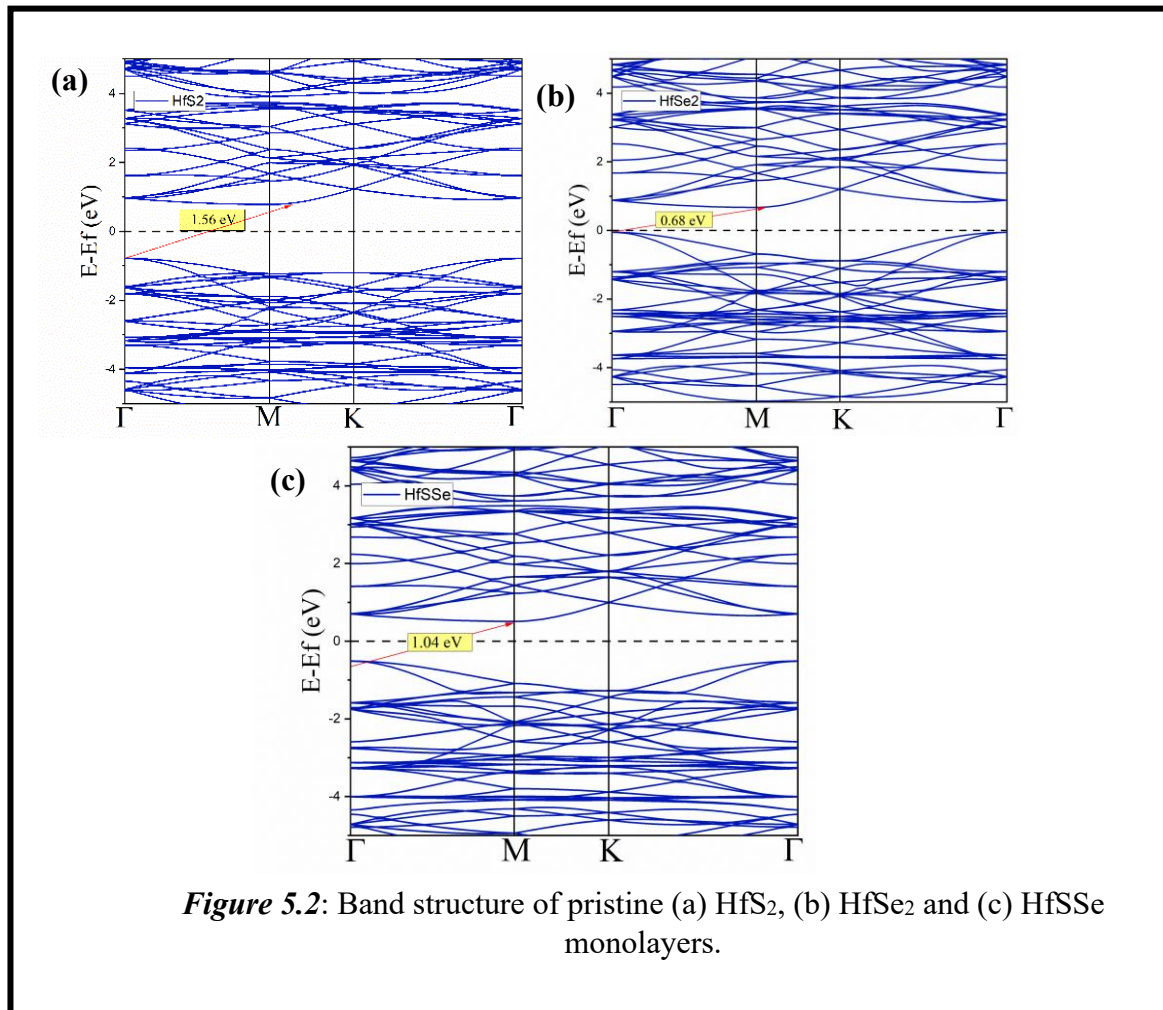


Figure 5.2: Band structure of pristine (a) HfS₂, (b) HfSe₂ and (c) HfSSe monolayers.

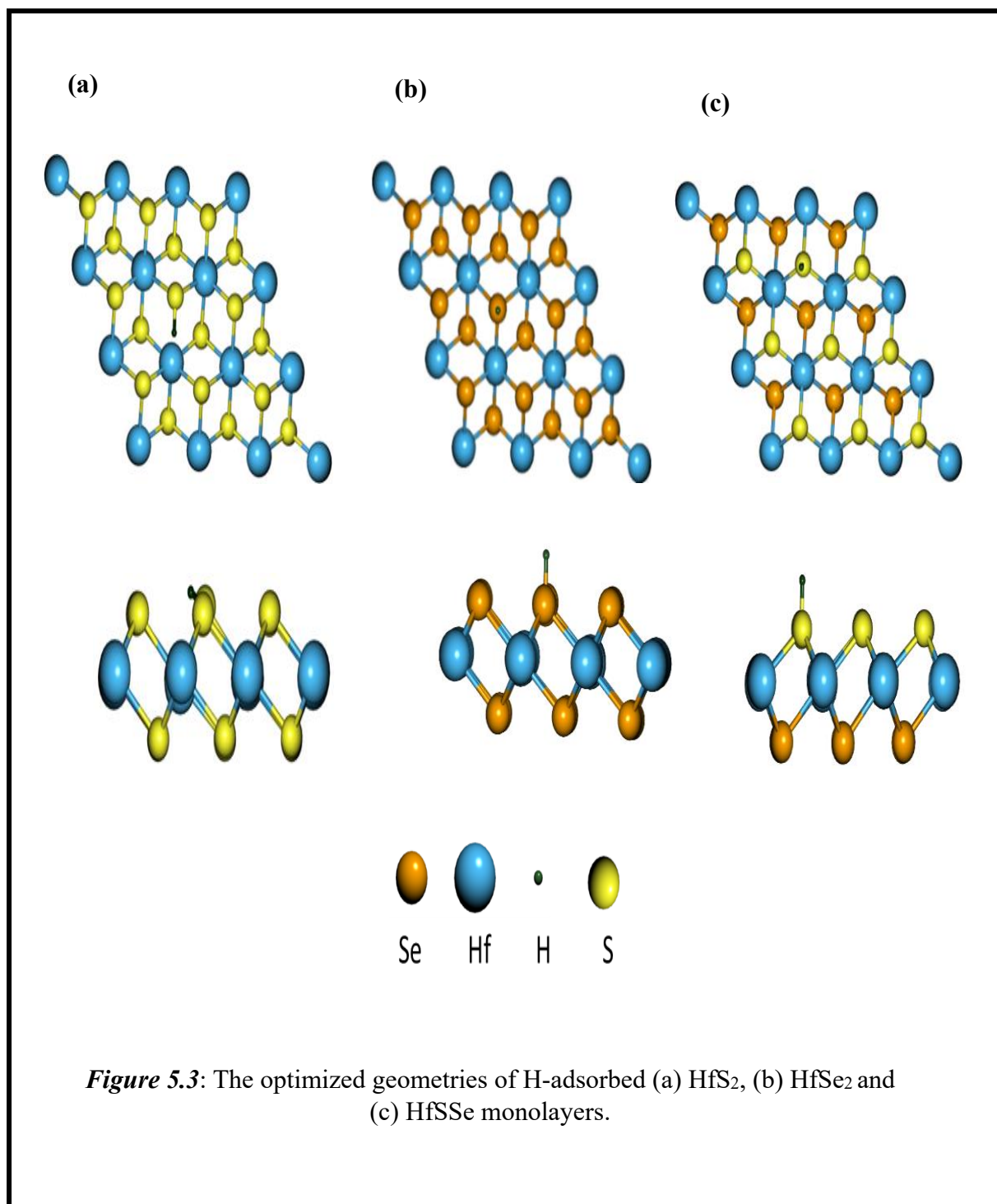


Table 5.2: Calculated ΔE_{ads}^H and ΔG^H of HER activity over pristine HfS₂, HfSe₂ and HfSSe monolayers.

Systems	Adsorption Site	ΔE_H (eV)	ΔG_H (eV)	Lowdin charge	
				$Q_H(e)$	$\Delta Q_H(e)$
HfS₂	Hf	1.85	2.09	1.28	0.28
	S	1.39	1.63	1.26	0.26
HfSe₂	Hf	1.56	1.80	1.41	0.41
	Se	1.44	1.68	1.23	0.23
HfSSe	Hf (Se-plane)	1.57	1.81	1.28	0.28
	Hf (S-plane)	1.85	2.09	1.34	0.34
	S-edge	1.16	1.40	1.17	0.17
	Se-edge	1.48	1.72	1.23	0.23

Table 5.3: Calculated lattice, bond lengths, ΔE_{ads}^H and ΔG^H of defected HfS₂, HfSe₂ and HfSSe monolayers.

Systems	Lattice constant (Å)	Bond length (Å)	Adsorption site	ΔE_H (eV)	ΔG_H (eV)	ΔQ_H (eV)
HfS₂-V_{Hf}	10.92	2.58	Hf	-0.20	0.04	0.30
HfS₂-V_S	10.93	2.58	Hollow	-1.21	-0.98	0.63
HfSe₂-V_{Hf}	11.11	2.70	Hollow	-0.02	0.21	0.42
HfSe₂-V_{Se}	11.15	2.67	Hf (move to hollow site)	-1.29	-1.05	0.70
HfSSe-V_{Hf}	11.03	2.42 (Hf-S) 2.68 (Hf-Se)	S	0.01	0.25	0.17
HfSSe-V_S	11.05	2.57 (Hf-S) 2.68 (Hf-Se)	Hf	-1.23	-0.99	0.34
HfSSe-V_{Se}	11.03	2.57 (Hf-S) 2.68 (Hf-Se)	Hollow	-1.19	-0.95	0.68

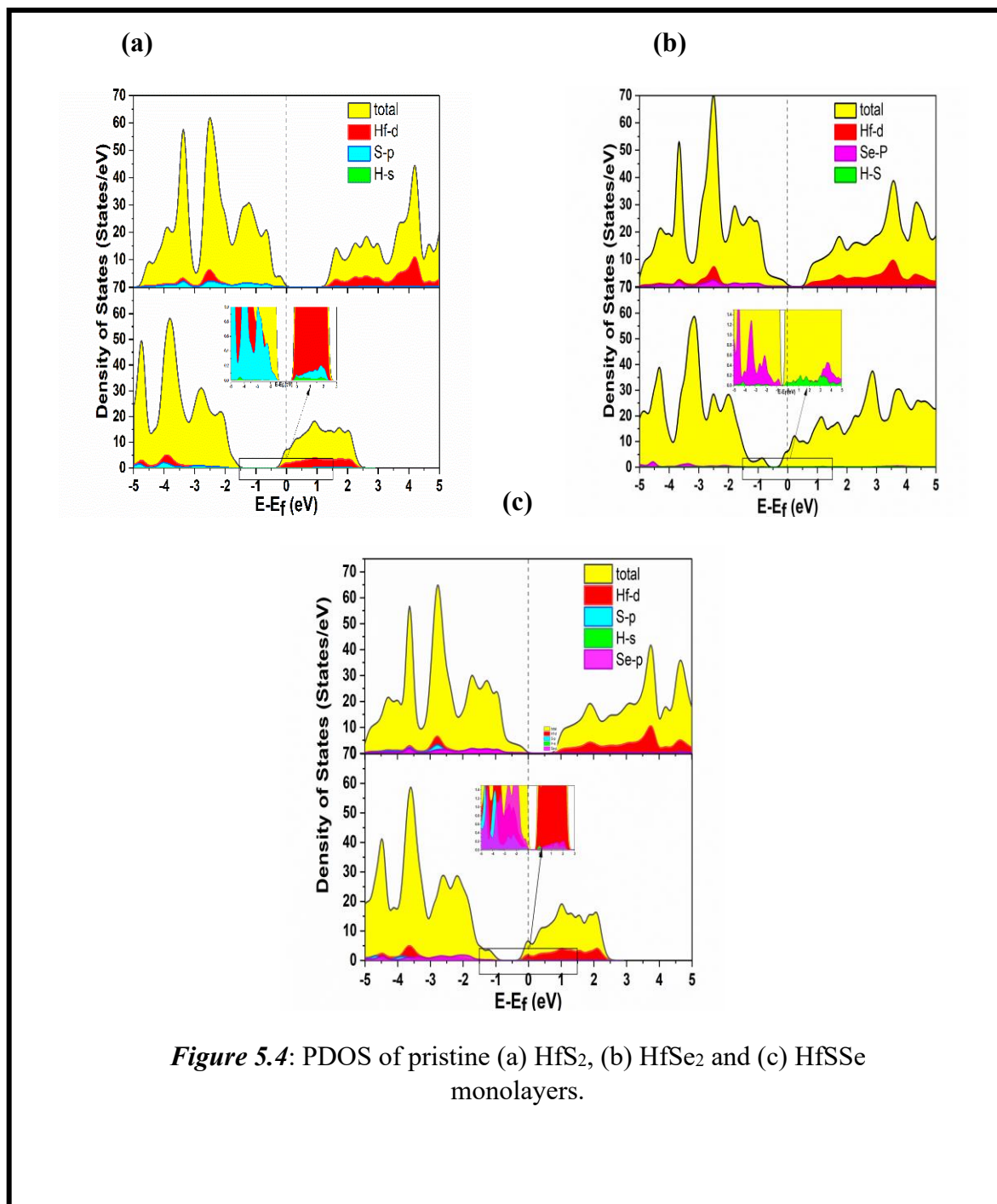
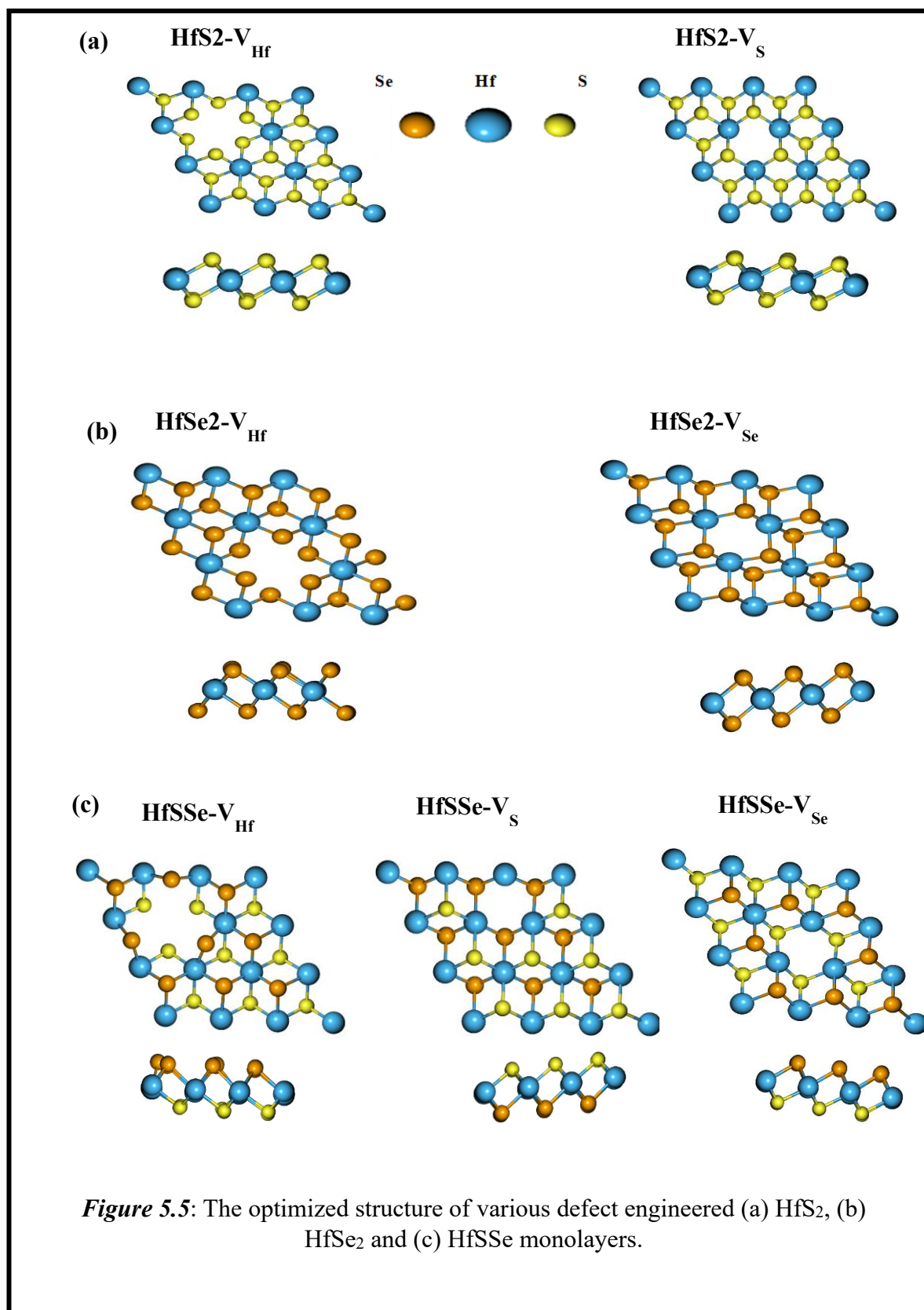


Figure 5.4: PDOS of pristine (a) HfS_2 , (b) HfSe_2 and (c) HfSSe monolayers.



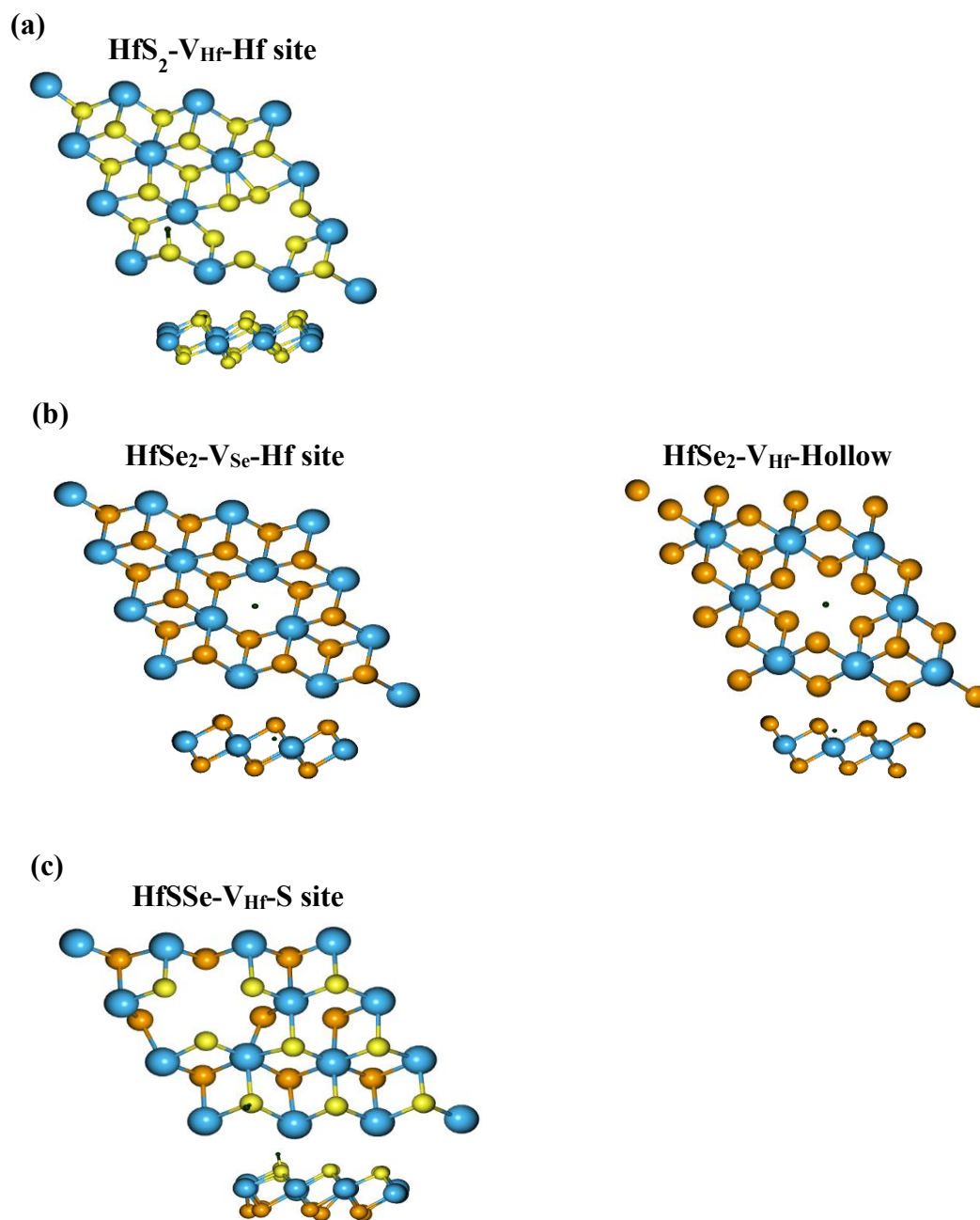


Figure 5.6: The optimized structures of H-adsorption on various defect engineered (a) HfS_2 , (b) HfSe_2 and (c) HfSSe monolayers.

Table 5.4: The comparison of ΔG^H of all stable 2D-TMDs (Ref. [86] with HfS₂ and HfSe₂ monolayers. (Our Work)

TMX ₂	(TMX ₂) $\Delta G_{H^*}(\text{eV})$	(TM-vacancy) $\Delta G_{H^*}(\text{eV})$	(X-vacancy) $\Delta G_{H^*}(\text{eV})$
CoTe ₂	-0.17	-0.15	-0.21
FeS ₂	0.13	-0.25	-0.01
CrS ₂	-0.11	-0.2	0.18
CrTe ₂	-0.14	-0.19	0.28
CrSe ₂	-0.11	-0.19	0.03
NiS ₂	-0.06	-0.22	-0.25
VS ₂	0.08	0.15	0.25
TaS ₂	0.18	-0.23	-0.1
NbS ₂	0.21	-0.18	0.23
NiTe ₂	0.21	-0.12	0.14
MnS ₂	0.15	-0.28	0.00
VSe ₂	0.24	0.11	0.04
NbSe ₂	0.25	-0.13	-0.16
VTe ₂	0.2	0.23	0.22
NbTe ₂	0.41	0.15	0.24
TiSe ₂	0.26	-0.16	0.18
TaSe ₂	0.24	-0.22	0.21
PdTe ₂	0.77	-0.05	0.15
TiTe ₂	0.4	0.14	0.06
TaTe ₂	0.33	0.2	0.4
MoTe ₂	-0.15	-0.12	0.13
ZrTe ₂	1.06	0.08	0.3
HfTe ₂	1.16	0.11	0.47
CoS ₂	-0.12	--	--
HfS ₂	1.63	0.04	-0.98
HfSe ₂	1.68	0.21	-1.05

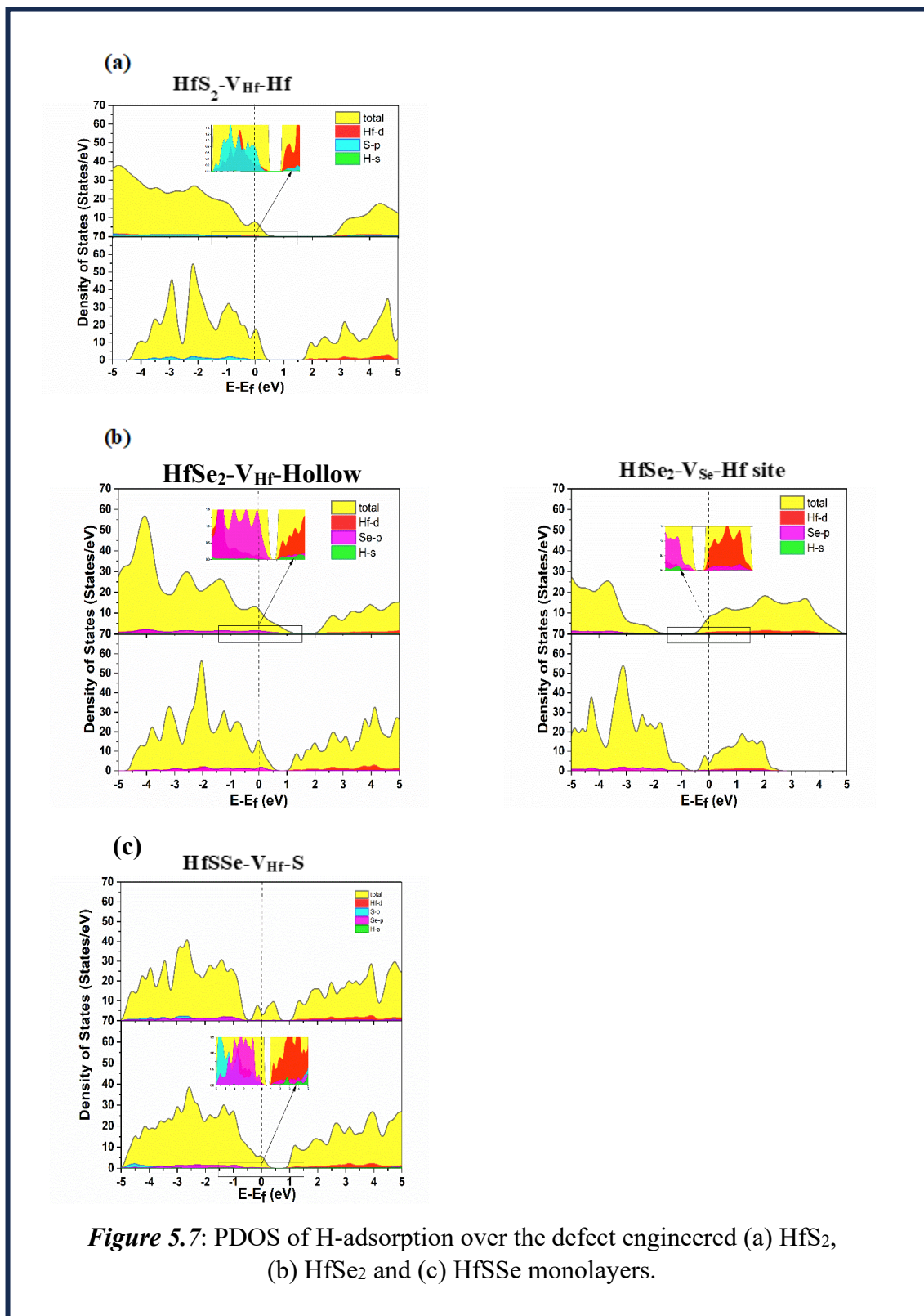
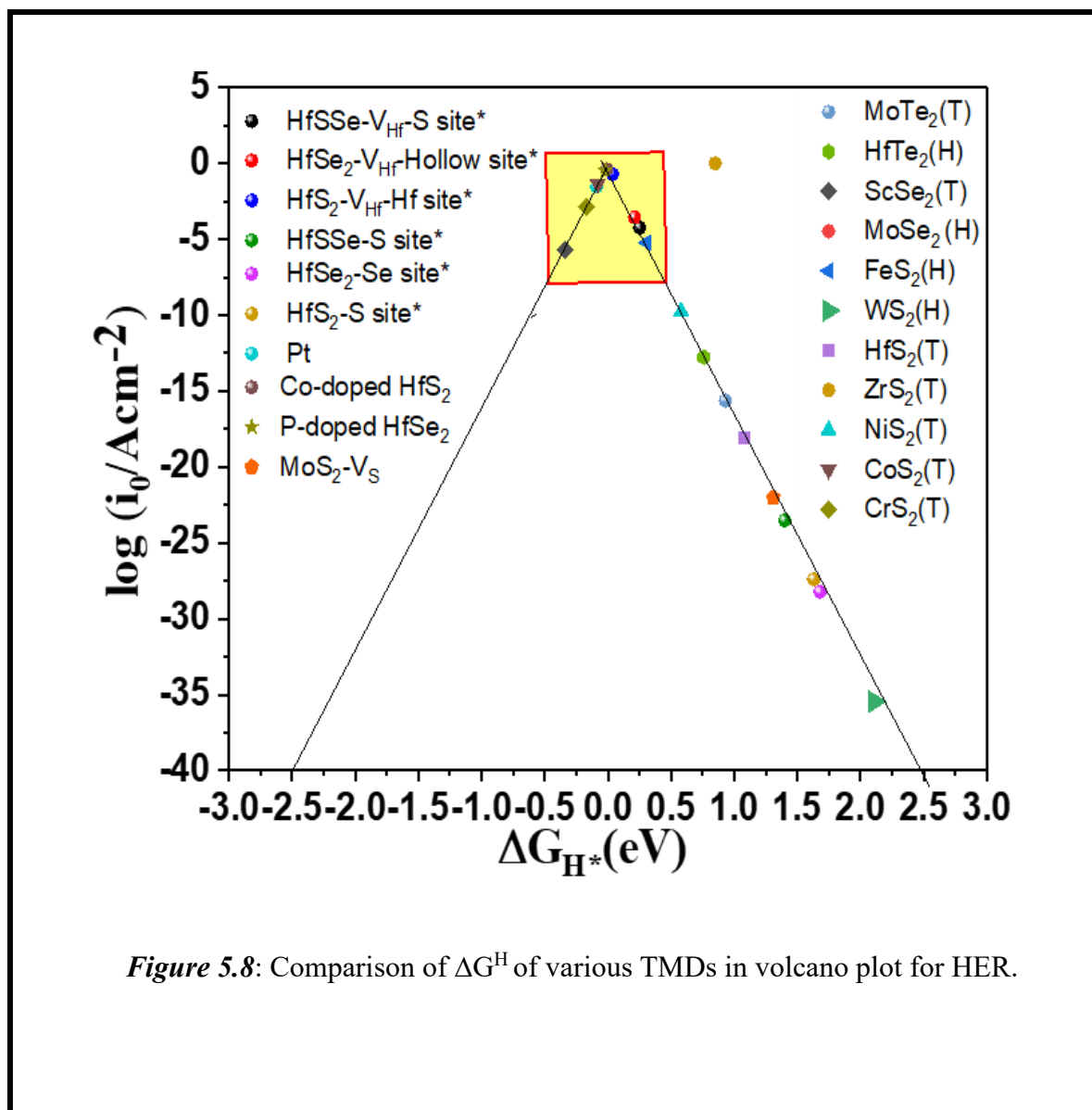


Figure 5.7: PDOS of H-adsorption over the defect engineered (a) HfS_2 , (b) HfSe_2 and (c) HfSSe monolayers.



5.4 Conclusion

In our investigation, we delved into the structural and electronic properties of HfS_2 , HfSe_2 and Janus HfSSe , with a specific focus on their potential as catalysts for HER. Our calculations unveiled that HfS_2 and HfSSe possess electronic band gaps of 1.56 eV and 1.04 eV, respectively, making them attractive candidates for deployment as photocatalysts. Conversely, HfSe_2 exhibited a narrower band gap of 0.68 eV, hinting at its suitability as an electrocatalyst.

To evaluate their catalytic prowess, we computed $\Delta E_{\text{ads}}^{\text{H}}$ and ΔG^{H} for H. Our results indicated that the Janus structure, akin to what was observed in Janus SeMoS, exhibited promising catalytic performance for the HER. Specifically, the order of hydrogen adsorption efficiency was as follows: HfSSe > HfS₂ > HfSe₂. To further enhance their catalytic efficiency, we introduced various defects into these materials, which significantly influenced their electronic properties. In the case of HfS₂, we observed that the presence of a vacancy V_{Hf} resulted in a lower ΔG^{H} when compared to the presence of a vacancy V_S or the pristine structure. Similarly, for HfSe₂, V_{Hf} exhibited lower ΔG^{H} values compared to V_{Se} or the pristine structure. Regarding Janus HfSSe, V_{Hf} displayed the lowest ΔG^{H} , followed by V_{Se} and V_S. Our analysis suggested that defected HfS₂ exhibited the most favourable ΔG^{H} , followed by defected HfSe₂ and defected Janus HfSSe, with values of 0.03 eV, 0.21 eV, and 0.25 eV, respectively. These observations lead to the conclusion that V_{Hf} in HfS₂ is particularly well-suited for the HER, as its value approaches the ideal value. In summary, our study underscores the significant role of defects in enhancing the catalytic performance of TMDs.

References

1. K. S. Novoselov, A. K. Geim, S. V. Morozov, D. Jiang, M. I. Katsnelson, I. V. Grigorieva, S. V. Dubonos and A. A. Firsov, *Nature*, 2005, **438**, 197–200.
2. V. P. Gusynin and S. G. Sharapov, *Phys Rev Lett*, 2005, **95**, 146801.
3. M. Khalid Butt, H. Muhammad Zeeshan, V. An Dinh, Y. Zhao, S. Wang and K. Jin, *Comput Mater Sci*, 2021, **197**, 110617.
4. N. M. R. Peres, *Rev Mod Phys*, 2010, **82**, 2673–2700.
5. B. Dunn, H. Kamath and J.-M. Tarascon, *Science (1979)*, 2011, **334**, 928–935.
6. Z. Yang, J. Zhang, M. C. W. Kintner-Meyer, X. Lu, D. Choi, J. P. Lemmon and J. Liu, *Chem Rev*, 2011, **111**, 3577–3613.
7. Q. Zhu, Y. Qu, D. Liu, K. W. Ng and H. Pan, *ACS Appl Nano Mater*, 2020, **3**, 6270–6296.
8. Urban, F. and Mitchell, T., (2011).
9. Z. W. Seh, J. Kibsgaard, C. F. Dickens, I. Chorkendorff, J. K. Nørskov and T. F. Jaramillo, *Science (1979)*, 2017, **355**.

10. J. Wang, Y. Gao, H. Kong, J. Kim, S. Choi, F. Ciucci, Y. Hao, S. Yang, Z. Shao and J. Lim, *Chem Soc Rev*, 2020, **49**, 9154–9196.
11. M. MOMIRLAN and T. VEZIROGLU, *Int J Hydrogen Energy*, 2005, **30**, 795–802.
12. T. Bak, J. Nowotny, M. Rekas and C. C. Sorrell, *Int J Hydrogen Energy*, 2002, **27**, 991–1022.
13. B. Sørensen and G. Spazzafumo, in *Hydrogen and Fuel Cells*, Elsevier, 2018, pp. 107–220.
14. A. Eftekhari, *Int J Hydrogen Energy*, 2017, **42**, 11053–11077.
15. R. Li and C. Li, 2017, pp. 1–57.
16. J. Di, C. Yan, A. D. Handoko, Z. W. Seh, H. Li and Z. Liu, *Materials Today*, 2018, **21**, 749–770.
17. J. D. Benck, T. R. Hellstern, J. Kibsgaard, P. Chakthranont and T. F. Jaramillo, *ACS Catal*, 2014, **4**, 3957–3971.
18. L. Mascaretti, S. Ferrulli, P. Mazzolini, C. S. Casari, V. Russo, R. Matarrese, I. Nova, G. Terraneo, N. Liu, P. Schmuki and A. Li Bassi, *Solar Energy Materials and Solar Cells*, 2017, **169**, 19–27.
19. D. P. Kumar, V. D. Kumari, M. Karthik, M. Sathish and M. V. Shankar, *Solar Energy Materials and Solar Cells*, 2017, **163**, 113–119.
20. M. Alizadeh, G. B. Tong, M. S. Mehmood, K. W. Qader, S. A. Rahman and B. Shokri, *Solar Energy Materials and Solar Cells*, 2018, **185**, 445–455.
21. I. Roger, M. A. Shipman and M. D. Symes, *Nat Rev Chem*, 2017, **1**, 0003.
22. A. N. Inamdar, N. N. Som, A. Pratap and P. K. Jha, *Int J Hydrogen Energy*, 2020, **45**, 18657–18665.
23. J. Kibsgaard and I. Chorkendorff, *Nat Energy*, 2019, **4**, 430–433.
24. M. S. Faber and S. Jin, *Energy Environ. Sci.*, 2014, **7**, 3519–3542.
25. X. Zou and Y. Zhang, *Chem Soc Rev*, 2015, **44**, 5148–5180.
26. B. Hinnemann, P. G. Moses, J. Bonde, K. P. Jørgensen, J. H. Nielsen, S. Horch, I. Chorkendorff and J. K. Nørskov, *J Am Chem Soc*, 2005, **127**, 5308–5309.
27. T. F. Jaramillo, K. P. Jørgensen, J. Bonde, J. H. Nielsen, S. Horch and I. Chorkendorff, *Science (1979)*, 2007, **317**, 100–102.
28. M. Chhowalla, H. S. Shin, G. Eda, L.-J. Li, K. P. Loh and H. Zhang, *Nat Chem*, 2013, **5**, 263–275.
29. D. Merki, H. Vrubel, L. Rovelli, S. Fierro and X. Hu, *Chem Sci*, 2012, **3**, 2515.
30. J. D. Benck, T. R. Hellstern, J. Kibsgaard, P. Chakthranont and T. F. Jaramillo, *ACS Catal*, 2014, **4**, 3957–3971.

31. H. Vrubel and X. Hu, *Angewandte Chemie International Edition*, 2012, **51**, 12703–12706.
32. D. Merki, H. Vrubel, L. Rovelli, S. Fierro and X. Hu, *Chem Sci*, 2012, **3**, 2515.
33. D. Kong, H. Wang, J. J. Cha, M. Pasta, K. J. Koski, J. Yao and Y. Cui, *Nano Lett*, 2013, **13**, 1341–1347.
34. H. Wang, D. Kong, P. Johannes, J. J. Cha, G. Zheng, K. Yan, N. Liu and Y. Cui, *Nano Lett*, 2013, **13**, 3426–3433.
35. H. Vrubel and X. Hu, *Angewandte Chemie International Edition*, 2012, **51**, 12703–12706.
36. W.-F. Chen, C.-H. Wang, K. Sasaki, N. Marinkovic, W. Xu, J. T. Muckerman, Y. Zhu and R. R. Adzic, *Energy Environ Sci*, 2013, **6**, 943.
37. W.-F. Chen, K. Sasaki, C. Ma, A. I. Frenkel, N. Marinkovic, J. T. Muckerman, Y. Zhu and R. R. Adzic, *Angewandte Chemie International Edition*, 2012, **51**, 6131–6135.
38. E. J. Popczun, J. R. McKone, C. G. Read, A. J. Biacchi, A. M. Wiltrout, N. S. Lewis and R. E. Schaak, *J Am Chem Soc*, 2013, **135**, 9267–9270.
39. Y. Ding, Y. Wang, J. Ni, L. Shi, S. Shi and W. Tang, *Physica B Condens Matter*, 2011, **406**, 2254–2260.
40. Y. Yi, Z. Chen, X. Yu, Z. Zhou and J. Li, *Adv Quantum Technol*, 2019, **2**.
41. R. S. El-Emam and H. Özcan, *J Clean Prod*, 2019, **220**, 593–609.
42. W. Zhang and K. Zhou, *Small*, 2017, **13**, 1700806.
43. H. Jin, C. Guo, X. Liu, J. Liu, A. Vasileff, Y. Jiao, Y. Zheng and S.-Z. Qiao, *Chem Rev*, 2018, **118**, 6337–6408.
44. Y. Chen, K. Yang, B. Jiang, J. Li, M. Zeng and L. Fu, *J Mater Chem A Mater*, 2017, **5**, 8187–8208.
45. Y. Jia, J. Chen and X. Yao, *Mater Chem Front*, 2018, **2**, 1250–1268.
46. C. Tang and Q. Zhang, *Advanced Materials*, 2017, **29**, 1604103.
47. R. J. Toh, Z. Sofer and M. Pumera, *J Mater Chem A Mater*, 2016, **4**, 18322–18334.
48. H. Cui, P. Jia and X. Peng, *Appl Surf Sci*, 2020, **513**, 145863.
49. H.-Y. Song, J.-J. Sun and M. Li, *Chem Phys Lett*, 2021, **784**, 139109.
50. K. O. Obodo, G. Gebreyesus, C. N. M. Ouma, J. T. Obodo, S. O. Ezeonu, D. P. Rai and B. Bouhafs, *RSC Adv*, 2020, **10**, 15670–15676.
51. M. Faghihnasiri, A. Ahmadi, S. Alvankar Golpayegan, S. Garosi Sharifabadi and A. Ramazani, *Nanomaterials*, 2020, **10**, 446.
52. M. Salavati, *Frontiers of Structural and Civil Engineering*, 2019, **13**, 486–494.
53. M. Barhoumi, K. Lazaar, S. Bouzidi and M. Said, *J Mol Graph Model*, 2020, **96**, 107511.

-
54. J. Hu, Q. Zhang, Q. Zhang and H. Cui, *Journal of Materials Research and Technology*, 2022, **20**, 763–771.
55. D. M. Hoat, M. Naseri, N. N. Hieu, R. Ponce-Pérez, J. F. Rivas-Silva, T. V. Vu and G. H. Coccoletzi, *Journal of Physics and Chemistry of Solids*, 2020, **144**, 109490.
56. D. L. Greenaway and R. Nitsche, *Journal of Physics and Chemistry of Solids*, 1965, **26**, 1445–1458.
57. M. Moustafa, T. Zandt, C. Janowitz and R. Manzke, *Phys Rev B*, 2009, **80**, 035206.
58. H. Jiang, *J Chem Phys*, 2011, **134**.
59. P. Johari and V. B. Shenoy, *ACS Nano*, 2012, **6**, 5449–5456.
60. K. F. Mak and J. Shan, *Nat Photonics*, 2016, **10**, 216–226.
61. D. Qin, P. Yan, G. Ding, X. Ge, H. Song and G. Gao, *Sci Rep*, 2018, **8**, 2764.
62. F. K. Perkins, A. L. Friedman, E. Cobas, P. M. Campbell, G. G. Jernigan and B. T. Jonker, *Nano Lett*, 2013, **13**, 668–673.
63. D. Voiry, J. Yang and M. Chhowalla, *Advanced Materials*, 2016, **28**, 6197–6206.
64. J. Lee, J. Y. Park, E. B. Cho, T. Y. Kim, S. A. Han, T. Kim, Y. Liu, S. K. Kim, C. J. Roh, H. Yoon, H. Ryu, W. Seung, J. S. Lee, J. Lee and S. Kim, *Advanced Materials*, 2017, **29**, 1606667.
65. D. Yan, Y. Li, J. Huo, R. Chen, L. Dai and S. Wang, *Advanced Materials*, 2017, **29**, 1606459.
66. H. Lou, G. Yu, M. Tang, W. Chen and G. Yang, *ACS Appl Mater Interfaces*, 2022, **14**, 7836–7844.
67. P. Giannozzi, S. Baroni, N. Bonini, M. Calandra, R. Car, C. Cavazzoni, D. Ceresoli, G. L. Chiarotti, M. Cococcioni, I. Dabo, A. Dal Corso, S. de Gironcoli, S. Fabris, G. Fratesi, R. Gebauer, U. Gerstmann, C. Gougoussis, A. Kokalj, M. Lazzeri, L. Martin-Samos, N. Marzari, F. Mauri, R. Mazzarello, S. Paolini, A. Pasquarello, L. Paulatto, C. Sbraccia, S. Scandolo, G. Sclauzero, A. P. Seitsonen, A. Smogunov, P. Umari and R. M. Wentzcovitch, *Journal of Physics: Condensed Matter*, 2009, **21**, 395502.
68. J. P. Perdew, K. Burke and Y. Wang, *Phys Rev B*, 1996, **54**, 16533–16539.
69. S. Grimme, *J Comput Chem*, 2006, **27**, 1787–1799.
70. J. D. Pack and H. J. Monkhorst, *Phys Rev B*, 1977, **16**, 1748–1749.
71. R. Almeida, A. Banerjee, S. Chakraborty, J. Almeida and R. Ahuja, *ChemPhysChem*, 2018, **19**, 148–152.
72. D. Singh, S. Chakraborty and R. Ahuja, *ACS Appl Energy Mater*, 2019, **2**, 8441–8448.
73. D. Chodvadiya, N. N. Som, P. K. Jha and B. Chakraborty, *Int J Hydrogen Energy*, 2021, **46**, 22478–22498.

-
74. C. H. Lee, B. Jun and S. U. Lee, *RSC Adv*, 2017, **7**, 27033–27039.
75. C. Gong, H. Zhang, W. Wang, L. Colombo, R. M. Wallace and K. Cho, *Appl Phys Lett*, 2013, **103**.
76. J. Bera, A. Betal and S. Sahu, *J Alloys Compd*, 2021, **872**, 159704.
77. A. B. Laursen, A. S. Varela, F. Dionigi, H. Fanchiu, C. Miller, O. L. Trinhammer, J. Rossmeisl and S. Dahl, *J Chem Educ*, 2012, **89**, 1595–1599.
78. S. H. Mir, S. Chakraborty, J. Wärnå, S. Narayan, P. C. Jha, P. K. Jha and R. Ahuja, *Catal Sci Technol*, 2017, **7**, 687–692.
79. Y.-H. Fang, G.-F. Wei and Z.-P. Liu, *The Journal of Physical Chemistry C*, 2013, **117**, 7669–7680.
80. J. Di, C. Yan, A. D. Handoko, Z. W. Seh, H. Li and Z. Liu, *Materials Today*, 2018, **21**, 749–770.
81. A. Eftekhari and B. Fang, *Int J Hydrogen Energy*, 2017, **42**, 25143–25165.
82. J. Lee, S. Kang, K. Yim, K. Y. Kim, H. W. Jang, Y. Kang and S. Han, *J Phys Chem Lett*, 2018, **9**, 2049–2055.
83. J. Zhang, S. Jia, I. Kholmanov, L. Dong, D. Er, W. Chen, H. Guo, Z. Jin, V. B. Shenoy, L. Shi and J. Lou, *ACS Nano*, 2017, **11**, 8192–8198.
84. A. Teasdale, *Org Process Res Dev*, 2016, **20**, 1850–1854.
85. X.-Y. Gao, J.-M. Zhang, A. Ali, X.-M. Wei and Y.-H. Huang, *Thin Solid Films*, 2021, **732**, 138790.
86. N. Ran, B. Sun, W. Qiu, E. Song, T. Chen and J. Liu, *J Phys Chem Lett*, 2021, **12**, 2102–2111.